

# Resonant spectral cascade in pulsatile flow triggered by arterial geometry

Khalid M. Saqr

Mechanical Engineering Department, College of Engineering and Technology  
Arab Academy for Science, Technology and Maritime Transport  
Alexandria 1029, EGYPT

## Abstract

The increasing geometric complexity of arteries with age is a well-established risk factor for cardiovascular disease, yet the precise physical mechanisms by which geometry interacts with blood flow remain debated. While complex geometry is known to increase viscous resistance, its active role in modulating flow dynamics is not fully understood. Here we solve a mathematical model to show that arterial geometry can trigger a resonant transfer of energy to short-wavelength components of the flow. The investigation, conducted over a physiological range of Womersley numbers ( $Wo$ , a dimensionless measure of pulsation frequency), reveal a dual dynamic. The global wave energy consistently decays, confirmed by a negative growth rate ( $G \downarrow 0$ ), indicating that the flow does not become exponentially unstable. However, a spectral broadening ratio ( $R$ ), which quantifies the energy in high-wavenumber versus low-wavenumber modes, exhibits a sharp, non-monotonic peak at an intermediate  $Wo$ . This result identifies a resonant frequency at which geometry is maximally efficient at generating spectral complexity, even as the overall flow attenuates. These findings reframe the role of arterial geometry from a passive dissipator to an active modulator of the flow's spectral content, suggesting that spectral diagnostics could provide a sensitive marker for vascular health.

**Keywords:** *Hemodynamics; Pulsatile flow; Womersley; Nonlinear waves; Korteweg-de Vries equation; Parametric forcing; Spectral cascade.*

## Introduction

Blood flow in large arteries exhibits complex dynamics resulting from the interaction of pulsatile forcing, viscous dissipation, elastic wall response, and vessel geometry. High-resolution

computational fluid dynamics (CFD) and particle image velocimetry (PIV) experiments have demonstrated that these factors can lead to complex, turbulence-like flow states characterized by a spectral cascade of kinetic energy, even under physiologic conditions [1, 2]. Factors such as vessel curvature [3], wall compliance [4, 5], and pathologic features like stenosis [6] are known to fundamentally alter local shear distributions and energy transport.

Curved and torsional arteries are not passive conduits. Classical studies of pulsatile flow in curved pipes established that curvature generates Dean-type secondary vortices and periodic shifts in velocity profiles that reshape wall shear stress [7]. Later analyses of fully developed oscillatory flow quantified how curvature amplitude controls phase lag and energy loss [8]. Laboratory experiments confirmed that increasing Dean number intensifies cross-stream motion and introduces nonuniform damping along the wall [9]. More recently, canonical curved-cavity experiments demonstrated that the interaction between Reynolds, Dean, and Womersley numbers produces distinct vortex morphologies analogous to those in intracranial aneurysms [10]. Computational models of coronary flow further showed that geometric curvature directly influences fractional flow reserve and hemodynamic stability under pulsatile forcing [3, 11]. Collectively, these results highlight that geometry-induced dispersion and secondary flow development are central to the stability of arterial pulsations.

At the same time, surface topography contributes to damping and flow modulation. Numerical investigations revealed that fine-scale wall roughness modifies wall shear stress metrics and can alter the onset of unsteadiness even at physiological Reynolds numbers [12]. Multiscale CFD analyses confirmed that realistic surface irregularity and non-Newtonian rheology combine to shift pressure–velocity phase relationships [13]. A comprehensive review of Dean-vortex manipulation summarized how secondary vortices can be tuned or suppressed through geometric control, reinforcing the notion that geometry acts as an active regulator of flow dynamics rather than a fixed boundary condition [14].

These geometric effects depend strongly on the pulsation frequency parameterized by the Womersley number. A recent meta-analysis of in-vivo measurements established that Womersley numbers vary from below 1 in arterioles to above 20 in large arteries, leading to major changes in the balance of inertial and viscous effects [15]. At low Womersley number, curvature primarily enhances viscous damping; at intermediate to high values, it can introduce transient energy amplification and phase-shifted responses [16]. Floquet stability analysis of pulsatile flow in toroidal pipes confirmed that these transitions correspond to narrow instability bands where curvature-driven dispersion couples resonantly with the oscillatory base flow [17].

Despite these insights, most analyses remain computationally expensive and geometry-specific. Direct numerical simulations and full fluid–structure interaction models capture detailed stress fields but obscure the parametric structure of instability. A reduced theoretical framework that isolates geometry as a parametric excitation could reveal when curvature or

torsion injects, rather than dissipates, energy.

Fractional and nonlocal modeling provides a promising route toward this goal. Fractional-order blood-flow models capture long-memory and multiscale geometric effects that arise from roughness, tortuosity, and distributed compliance [18]. Comparative reviews show that fractional models reproduce arterial viscoelastic lag and pressure–flow hysteresis more accurately than classical formulations [19]. Recent works have combined fractional operators with data-driven or neural-network approaches to describe nonlinear flow behavior under physiological conditions [20]. These developments motivate a formulation that embeds fractional operators into stability analyses, allowing the same mathematical machinery to describe geometry-induced damping and amplification.

The present study builds directly upon this evolving paradigm by asking a simple but unresolved question: *can arterial geometry itself, independent of material and viscous effects, act as a source of dynamic instability in pulsatile flow?* Traditional hemodynamic models treat curvature and torsion as static modifiers of resistance or wave speed, yet emerging evidence suggests they can inject energy into the flow under certain pulsation conditions. Addressing this question requires a framework that isolates geometric forcing from constitutive or boundary effects while remaining tractable enough for broad parameter exploration.

Here we propose such a framework. Using a variable-coefficient fractional Korteweg–de Vries formulation, we recast curvature, torsion, and surface roughness as spatially modulated coefficients governing dispersion and dissipation. The model integrates fractional operators to represent distributed geometric memory and nonlocal damping, and we numerically simulate the resulting dynamics to identify parametric growth regimes across the physiological Womersley spectrum. The computational workflow links geometric modulation directly to measurable instability metrics, providing a reproducible map from geometry to wave growth or decay.

In this sense, the study challenges the prevailing view that viscous dissipation universally stabilizes pulsatile flow. It suggests instead that under specific combinations of curvature, torsion, and pulsation frequency, geometry can act as a *driver* rather than a *dissipator*. While variable-coefficient KdV models have been foundational in fields like nonlinear optics and shallow-water wave theory, the present work originally applies this framework to pulsatile hemodynamics. Our approach unifies classical curved-pipe hydrodynamics [7–9], modern computational hemodynamics [3, 12, 13], and fractional modeling theory [18–20] into a single analytical–computational pipeline. By turning geometry from a passive constraint into an active variable, this work reframes arterial stability as a question of parametric energy exchange, opening a new path for interpreting instability in pulsatile biological flows.

# Methods

This section derives a nonlinear one-dimensional model for pulsatile blood flow in geometrically complex arteries from the Navier–Stokes equations, followed by the computational workflow used for stability and chaos diagnostics.

## Governing Equations.

Let  $\rho$  [ $\text{kg m}^{-3}$ ] and  $\mu$  [ $\text{Pa s}$ ] denote blood density and dynamic viscosity. In cylindrical coordinates  $(r, \theta, z)$ , the velocity components are  $(v_r, v_\theta, v_z)$  [ $\text{m s}^{-1}$ ] and the pressure field is  $p$  [ $\text{Pa}$ ]. The incompressible Navier–Stokes system reads

$$\frac{1}{r} \frac{\partial}{\partial r} (r v_r) + \frac{1}{r} \frac{\partial v_\theta}{\partial \theta} + \frac{\partial v_z}{\partial z} = 0, \quad (1)$$

$$\rho \left( \frac{\partial v_z}{\partial t} + v_r \frac{\partial v_z}{\partial r} + \frac{v_\theta}{r} \frac{\partial v_z}{\partial \theta} + v_z \frac{\partial v_z}{\partial z} \right) = -\frac{\partial p}{\partial z} + \mu \left[ \frac{1}{r} \frac{\partial}{\partial r} \left( r \frac{\partial v_z}{\partial r} \right) + \frac{1}{r^2} \frac{\partial^2 v_z}{\partial \theta^2} + \frac{\partial^2 v_z}{\partial z^2} \right]. \quad (2)$$

For straight, axisymmetric vessels ( $\partial/\partial\theta = 0, v_\theta = 0$ ), Eq. (2) simplifies to

$$\rho \left( \frac{\partial v_z}{\partial t} + v_r \frac{\partial v_z}{\partial r} + v_z \frac{\partial v_z}{\partial z} \right) = -\frac{\partial p}{\partial z} + \mu \left[ \frac{1}{r} \frac{\partial}{\partial r} \left( r \frac{\partial v_z}{\partial r} \right) \right]. \quad (3)$$

**Base Oscillatory (Womersley) Flow:** Neglecting convective terms in Eq. (3) gives the linear unsteady Stokes equation. For a harmonic pressure gradient  $\partial p/\partial z = \Re\{\hat{P}e^{i\omega t}\}$ , the exact velocity solution is

$$v_0(r, t) = \Re \left[ \frac{\hat{P}}{i\rho\omega} \left( 1 - \frac{J_0(i^{3/2}\text{Wo} r/R_0)}{J_0(i^{3/2}\text{Wo})} \right) e^{i\omega t} \right], \quad (4)$$

where  $\text{Wo} = R_0 \sqrt{\omega/\nu}$  is the Womersley number,  $\nu = \mu/\rho$ , and  $J_0$  is the Bessel function of the first kind. This oscillatory profile forms the base state for subsequent perturbation analysis.

**Weakly Nonlinear Reduction:** To capture finite-amplitude effects neglected by Eq. (4), we expand the axial velocity as

$$v_z(r, x, t) = v_0(r, t) + \epsilon A(x, t) \phi(r) + \mathcal{O}(\epsilon^2), \quad (5)$$

where  $x$  is the centerline coordinate,  $\epsilon \ll 1$  is a small parameter,  $A(x, t)$  is the slowly varying wave amplitude, and  $\phi(r)$  is the normalized radial eigenfunction of the linear operator from Eq. (3). Substituting Eq. (5) into Eq. (3), projecting onto  $\phi(r)$ , and retaining  $\mathcal{O}(\epsilon^2)$  terms

yields the amplitude evolution equation

$$\frac{\partial A}{\partial t} + C(x)A\frac{\partial A}{\partial x} + D(x)\frac{\partial^3 A}{\partial x^3} + K(x)\mathcal{D}^{\gamma(x)}A = 0. \quad (6)$$

The nonlinear term  $C(x)A(\partial A/\partial x)$  arises directly from the convective acceleration  $v_z(\partial v_z/\partial z)$  in Eq. (3) and represents amplitude-dependent wave steepening. The dispersive coefficient  $D(x)$  comes from higher-order viscous and geometric corrections, and  $K(x)\mathcal{D}^{\gamma(x)}A$  models distributed geometric damping through the Riesz fractional derivative

$$\mathcal{F}[\mathcal{D}^{\gamma(x)}A] = |k|^{1+\gamma(x)}\hat{A}(k), \quad (7)$$

where  $\mathcal{F}$  denotes the Fourier transform.

## Dimensionless Form and Geometric Modulation.

Introducing scales  $L_0$ ,  $T_0 = 1/\omega$ ,  $A_0$ , and dimensionless variables  $\xi = x/L_0$ ,  $\tau = t/T_0$ ,  $a_1 = A/A_0$ , gives

$$\frac{\partial a_1}{\partial \tau} + \alpha_0 a_1 \frac{\partial a_1}{\partial \xi} + \beta(\xi) \frac{\partial^3 a_1}{\partial \xi^3} + \eta(\xi) (-\partial_\xi^2)^{\frac{1+\gamma_0}{2}} a_1 = 0, \quad (8)$$

with  $\alpha_0$ ,  $\beta(\xi)$ , and  $\eta(\xi)$  representing nonlinearity, dispersion, and damping. The general form includes a Riesz fractional operator, but for this study, the order was fixed to  $\gamma_0 = 0$ , which reduces the operator to a form proportional to the standard viscous term. The nonlinearity was held constant ( $\alpha_0 = 1$ ). Periodic spatial modulations mimic curvature or torsion:

$$\beta(\xi) = \beta_0[1 + \varepsilon_\beta \cos(q\xi)], \quad \eta(\xi) = \eta_0[1 + \varepsilon_\eta \cos(q\xi)],$$

where  $q$  is the geometric wavenumber and  $\varepsilon_i$  are modulation amplitudes ( $0 \leq \varepsilon_i \leq 0.3$ ). The baseline scalings are physically motivated:  $\beta_0 \propto \text{Wo}^{-2}$  arises from the balance of inertial and viscous effects in the underlying Womersley flow, while  $\eta_0 = \eta_{\text{ref}}(1 + 0.1/\text{Wo})$  models frequency-dependent dissipation from viscous boundary layers, with a reference damping value of  $\eta_{\text{ref}} = 0.005$ .

**Initial and Boundary Conditions:** The system is solved on a periodic domain of length  $L_g$ . The initial condition is a physiologically informed multi-harmonic waveform given by  $a_1(\xi, 0) = \sum_{n=1}^3 A_n \sin(nk_0\xi + \phi_n)$  with amplitude ratios  $A_2/A_1 = 0.3$  and  $A_3/A_1 = 0.1$ . For the detailed representative case shown in Figures 2-6, a fundamental wavenumber of  $k_0 = 0.5$  was used. For the parametric sweep summarized in Figures 7-9,  $k_0 = 1.0$  was used. The use of a Fourier-based solver inherently enforces periodic boundary conditions for all simulations.

**Parameter Range:** Simulations span  $\text{Wo} \in \{2, 5, 10, 15, 20\}$  and modulation amplitudes  $\varepsilon_i \leq 0.3$ . The dimensionless geometric period was held constant at  $qL_g = 4\pi$ . This range covers

small- to large-artery regimes [15] and conditions for curvature-driven resonance [16, 17].

**Numerical Integration Scheme:** Equation (8) is solved numerically using a split-step Fourier pseudospectral method. The domain of length  $L_g$  is discretized into  $N$  uniformly spaced points. The nonlinear term,  $-\alpha(\xi)a_1\partial_\xi a_1$ , is calculated in real space and advanced in time using a fourth-order Runge-Kutta scheme. The linear part, containing the dispersive and fractional damping terms, is handled in Fourier space.

For computational efficiency, the spatially-varying linear operator is approximated by using the spatial mean of the coefficients,  $\bar{\beta} = \langle \beta(\xi) \rangle$  and  $\bar{\eta} = \langle \eta(\xi) \rangle$ . This defines a constant-coefficient linear operator in Fourier space,  $L(k) = -i\bar{\beta}k^3 - \bar{\eta}|k|^{1+\gamma_0}$ . The solution is advanced each timestep by applying an exact exponential propagator based on this mean operator,  $\hat{a}_1(k, \tau + \Delta\tau) = e^{\Delta\tau L(k)}\hat{a}_1(k, \tau)$ . This approach robustly captures the average dispersive and damping effects while significantly improving numerical performance.

## Instability Diagnostics

To quantify the system's dynamics, we employ two primary diagnostics. First, the global energy of the wave is defined as  $I_2(\tau) = \int_0^{L_g} a_1^2 d\xi$ . Its instantaneous logarithmic growth rate,

$$G(\tau) = \frac{d}{d\tau} \ln I_2(\tau), \quad (9)$$

is used to identify periods of energy growth ( $G > 0$ ) or decay ( $G < 0$ ), signaling global stability.

Second, to measure the transfer of energy to small scales, we define the spectral broadening ratio,  $R(\tau)$ . This is the ratio of energy in high-wavenumber modes to that in low-wavenumber modes:

$$R(\tau) = \frac{E_{\text{high}}}{E_{\text{low}}} = \frac{\int_{k_c}^{k_{\text{max}}} |\hat{a}_1(k, \tau)|^2 dk}{\int_0^{k_c} |\hat{a}_1(k, \tau)|^2 dk},$$

where the cutoff wavenumber is defined relative to the initial condition's fundamental wavenumber as  $k_c = 1.5 \times (3k_0)$ , separating the initial energy-containing modes from the high-frequency cascade. A value of  $R > 1.5$  is taken as a threshold indicating a significant spectral cascade and the onset of a broadband, complex state.

The dimensionless amplitude  $a_1$  corresponds to physical velocity perturbation  $v'_z(x, t) = A_0 a_1(x/L_0, t/T_0)$ . In the limit  $\varepsilon_i = 0$  and  $\eta = 0$ , Eq. (8) recovers the integrable constant-coefficient KdV equation, conserving invariants  $I_1$  and  $I_3$ . The solver reproduces the analytical Womersley velocity field for vanishing nonlinearity, validating both physical and numerical consistency. All algorithms were implemented in Python using NumPy and FFTW; code and data are available for reproducibility.

## Solution Approach

The numerical solution of the governing equation is performed using the split-step Fourier pseudospectral scheme detailed above, implemented in Python. The core computations and Fast Fourier Transforms rely on the NumPy and SciPy libraries, while the parameter sweep results were managed with pandas and all figures were generated using Matplotlib. All spatial derivatives are evaluated spectrally, which inherently enforces the periodic boundary conditions. Temporal integration continues until the diagnostic quantities reach a quasi-steady state.

The solver is verified by confirming that it reproduces analytical solutions for the Korteweg-de Vries equation in the constant-coefficient limit ( $\varepsilon_i = 0$ ) and conserves the energy invariant  $I_2$  in the absence of damping ( $\eta = 0$ ). Numerical convergence was established by refining the spatial grid spacing  $\Delta\xi$  and timestep  $\Delta\tau$  until the relative change in the total energy  $I_2$  between runs was less than  $10^{-5}$ . The scheme does not employ an explicit de-aliasing procedure; however, an additional check for numerical accuracy was performed by monitoring the energy in the highest-wavenumber modes, which remained a negligible fraction of the total energy, providing confidence that aliasing errors did not contaminate the physical cascade. All source code and data are available to ensure full reproducibility. The key numerical and physical parameters used in the simulations are summarized in Table 1.

Table 1: Key simulation parameters used in the study.

Parameter	Symbol	Value
<i>Numerical Parameters</i>		
Number of Collocation Points	$N$	512
Dimensionless Domain Length	$L_g$	$4\pi$
Timestep (Exploratory Script)	$\Delta\tau$	$5 \times 10^{-5}$
Timestep (Sweep Script)	$\Delta\tau$	$2 \times 10^{-4}$
Final Time (Exploratory Script)	$T_{final}$	200.0
Final Time (Sweep Script)	$T_{final}$	60.0
<i>Physical and Geometric Parameters</i>		
Womersley Number Range	$Wo$	$\{2, 5, 10, 15, 20\}$
Dispersion Modulation Amplitude	$\varepsilon_\beta$	0.3
Damping Modulation Amplitude	$\varepsilon_\eta$	0.3
Fundamental Wavenumber (Figs 2–6)	$k_0$	0.5
Fundamental Wavenumber (Figs 7–9)	$k_0$	1.0
Geometric Wavenumber	$q$	1.0
Reference Damping	$\eta_{ref}$	0.005
Nonlinearity Coefficient	$\alpha_0$	1.0
Fractional Order	$\gamma_0$	0.0

# Results

The simulation was performed for a representative case with a Womersley number of  $Wo = 10$ . The initial conditions and spatially-modulated coefficients for this run are presented in Figure 1. The top panel shows the initial waveform,  $a_1(\xi, 0)$ , a composite of three harmonics resulting in an asymmetric profile with a dominant peak and a broader, shallower trough. The bottom panel displays the periodic functions for the dispersion coefficient,  $\beta(\xi)$ , and the damping coefficient,  $\eta(\xi)$ . Both coefficients vary in-phase with one another over two full geometric periods within the computational domain, establishing the spatially-dependent forcing of the system.

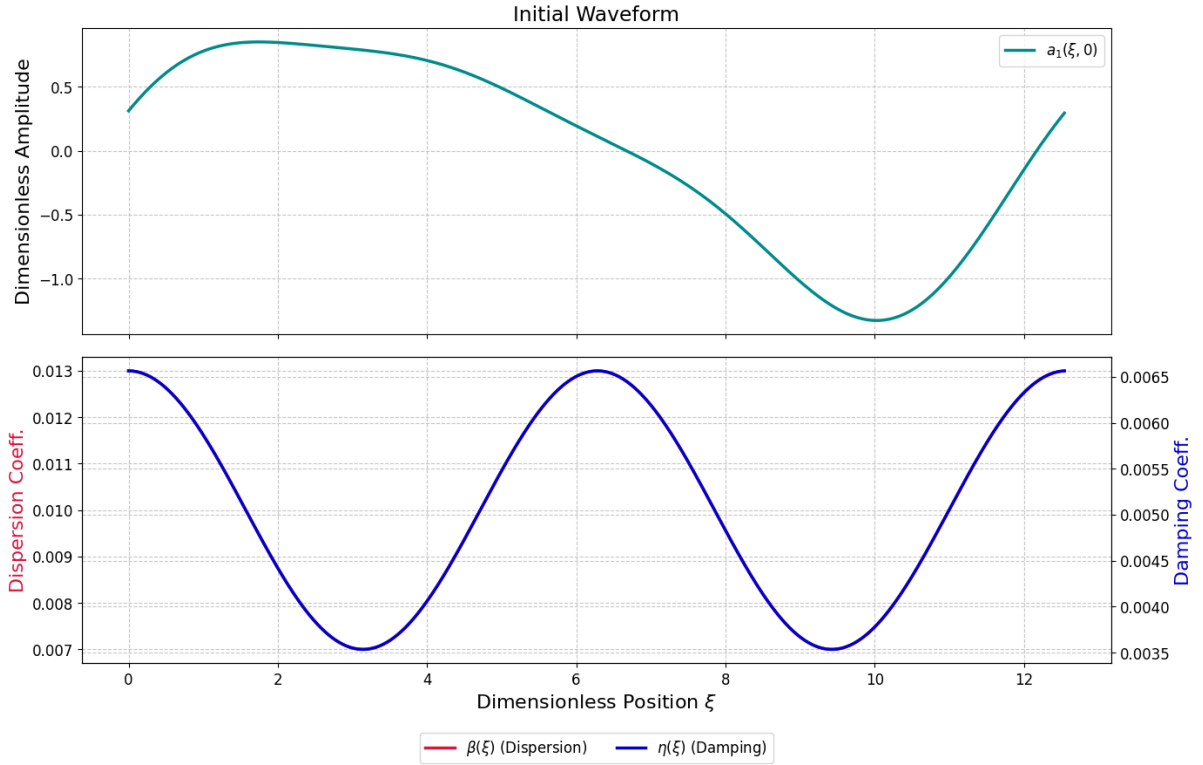


Figure 1: Initial setup for the simulation with  $Wo = 10$ . Top: The multi-harmonic initial waveform  $a_1(\xi, 0)$ . Bottom: The spatially-periodic dispersion coefficient  $\beta(\xi)$  (left axis, red) and damping coefficient  $\eta(\xi)$  (right axis, blue).

The global dynamics of the system are summarized by the primary instability diagnostics in Figure 2. As shown in the top panel, the total wave energy,  $I_2(\tau)$ , decays by approximately two orders of magnitude over the simulation, indicating that the system is globally stable. The middle panel confirms this, showing that the instantaneous growth rate,  $G(\tau)$ , remains negative for all time; it undergoes large oscillations initially before settling to a quasi-steady negative value. In stark contrast, the bottom panel reveals a highly transient, nonlinear process: the spectral broadening ratio,  $R(\tau)$ , exhibits a sharp peak reaching a value greater than 20 within

the first 40 time units. This demonstrates a rapid and significant transfer of energy to high wavenumbers that dramatically precedes the long-term energy decay.

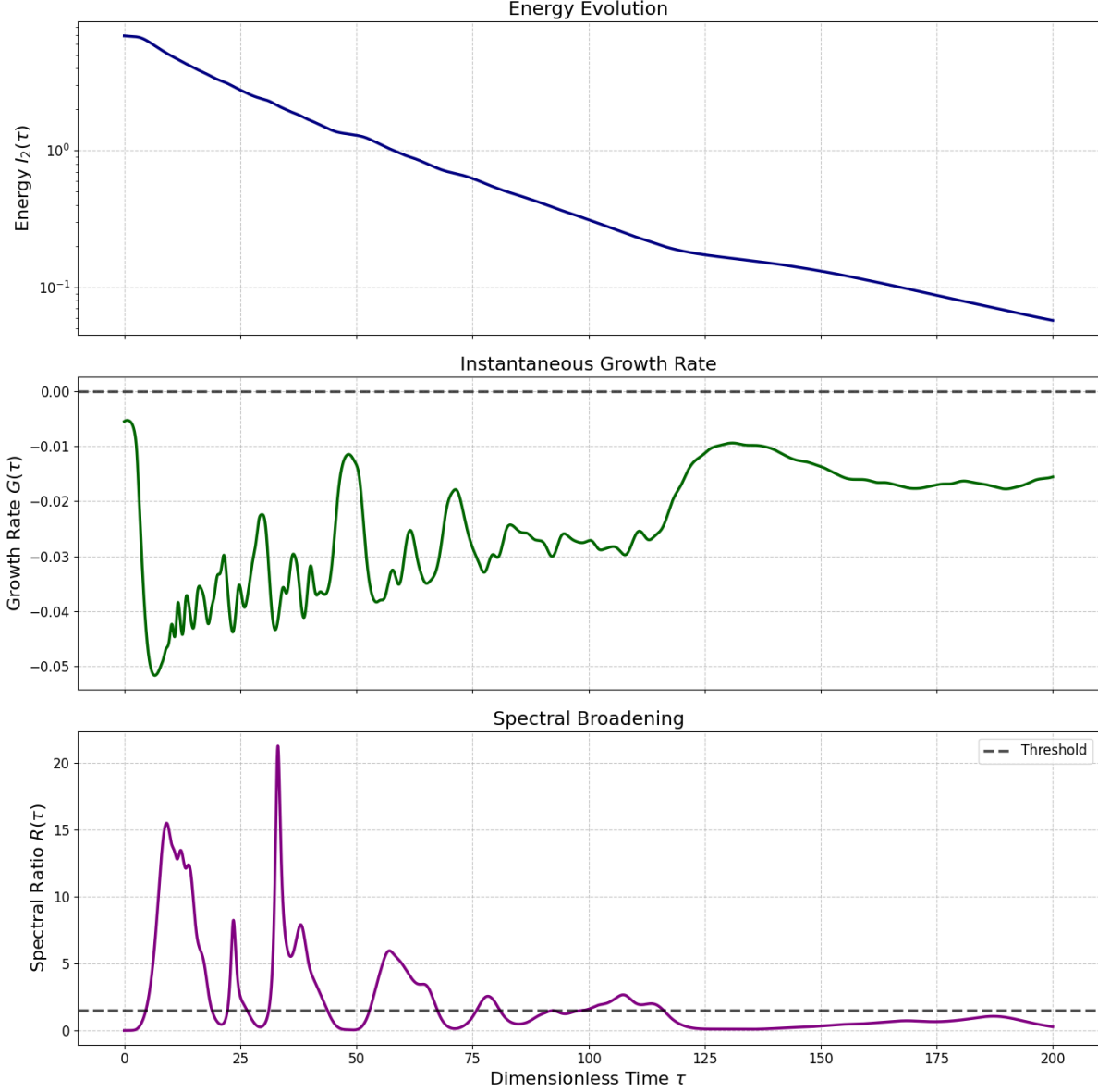


Figure 2: Primary instability diagnostics for  $\text{Wo} = 10$ . Top: Total wave energy  $I_2(\tau)$  on a semi-logarithmic scale. Middle: Instantaneous energy growth rate  $G(\tau)$ . Bottom: Spectral broadening ratio  $R(\tau)$ , with the broadband threshold indicated by the dashed line.

The mechanism of this energy transfer is detailed in Figure 3, which tracks the energy in the first five Fourier harmonics. The plot shows a rapid initial redistribution of energy, where all five modes achieve a state of near equipartition within the first few time units. Subsequently,

the energy in all tracked modes undergoes a coupled, fluctuating decay. No single mode exhibits sustained exponential growth, which is consistent with the global stability of the system.

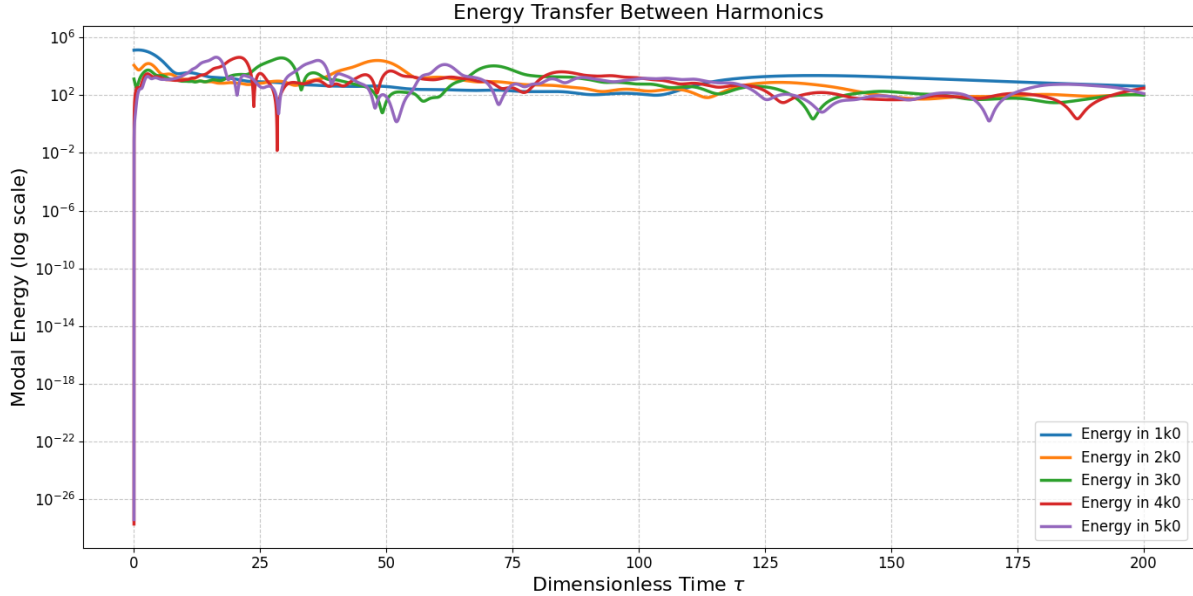


Figure 3: Modal energy evolution for the first five harmonics ( $k_0$  to  $5k_0$ ) for the  $Wo = 10$  case. The energy in each mode is plotted over time on a semi-logarithmic scale.

The physical effect of the transient energy cascade on the waveform's shape is visualized in the snapshots of Figure 4. The initially smooth profile at  $\tau = 0.0$  undergoes a dramatic transformation into the highly irregular waveform seen at  $\tau = 50.0$ , which is characterized by the emergence of numerous high-frequency oscillations and sharp gradients. The subsequent snapshots at  $\tau = 100.0$ ,  $150.0$ , and  $200.0$  illustrate a process of gradual damping, where both the overall amplitude and the fine-scale structures are progressively attenuated.

Figure 5 demonstrates the non-conservative nature of the system by tracking the evolution of the first and third classical KdV invariants. The momentum-like invariant,  $I_1$  (top panel), deviates immediately from its initial zero value and undergoes sustained, decaying oscillations around a negative mean. The higher-order invariant,  $I_3$  (bottom panel), experiences a sharp initial plunge before oscillating back towards a near-zero steady-state value. The dynamic behavior of both quantities confirms that the geometric terms are actively modulating the integral properties of the flow.

A comprehensive spatiotemporal overview of the simulation is provided in Figure 6. The top panel, showing  $a_1(\xi, \tau)$ , reveals that the initial, large-scale coherent wave structures break down into a complex field of smaller, interacting wave packets. The bottom panel presents the corresponding power spectrum evolution, or spectrogram. This plot clearly visualizes the nearly instantaneous transfer of energy from the initial discrete modes to a broad, continuous

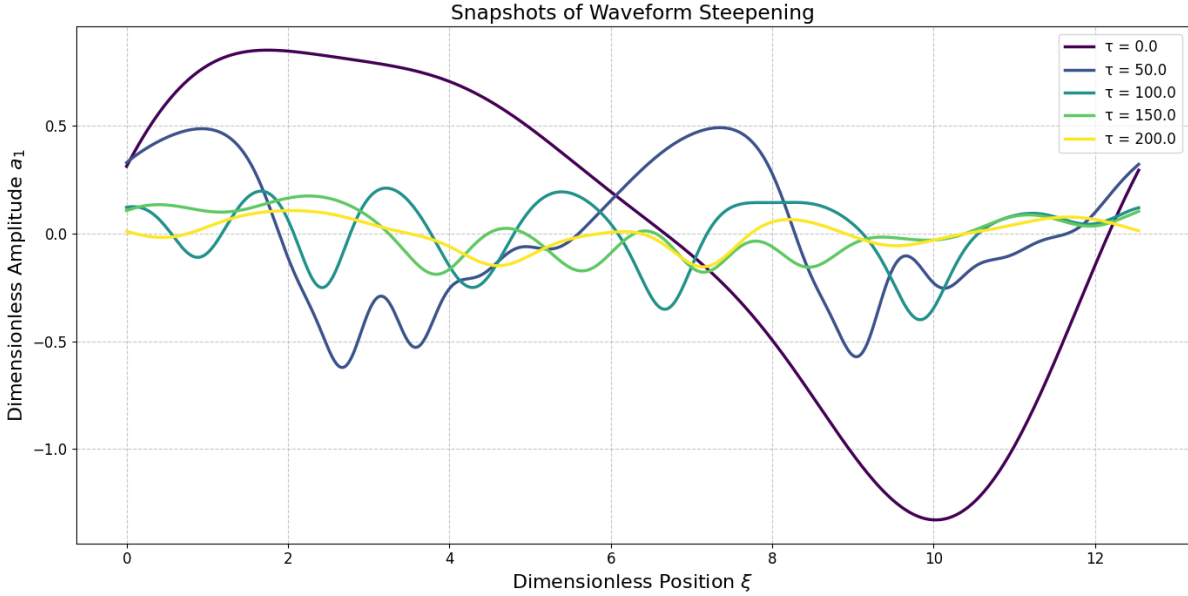


Figure 4: Waveform shape evolution at selected time snapshots for  $Wo = 10$ . The plot illustrates the development of high-frequency structures and the subsequent decay of the wave amplitude.

spectrum of wavenumbers. This broadband state persists while its overall intensity gradually fades, visually confirming the global, system-wide damping over time.

The summary of the parameter sweep across the physiological range of Womersley numbers is presented in Figure 7. The plot synthesizes the primary instability metrics as a function of  $Wo$ . The maximum late-stage growth rate,  $G$ , is plotted on the left vertical axis, while the maximum transient spectral broadening ratio,  $R$ , is plotted on the right. The results show that the growth rate  $G$  remains negative for all tested Womersley numbers, indicating that the system is globally stable across this range. The magnitude of the decay increases with  $Wo$ , suggesting stronger long-term damping at higher frequencies. In contrast, the spectral broadening ratio  $R$  exhibits a non-monotonic dependence on the Womersley number. It rises from a low value at  $Wo = 2$  to a distinct peak at  $Wo = 15$ , before decreasing again at  $Wo = 20$ . For all cases, the peak value of  $R$  remains significantly above the broadband threshold of 1.5.

The parametric dependence of the system's final state on the Womersley number is detailed in Figures 8 and 9. Figure 8 presents direct overlays of the final-state solutions. The top panel shows the final waveform,  $a_1(\xi, \tau_{final})$ , for each tested  $Wo$ . The final amplitude is a non-monotonic function of  $Wo$ , with the largest amplitude observed at  $Wo = 2$  and the smallest at  $Wo = 20$ . The waveform complexity, characterized by the prevalence of short-wavelength oscillations, appears greatest for intermediate Womersley numbers. The bottom panel displays the corresponding final power spectra,  $|\hat{a}_1(k, \tau_{final})|^2$ . All cases result in a broadband spectrum,

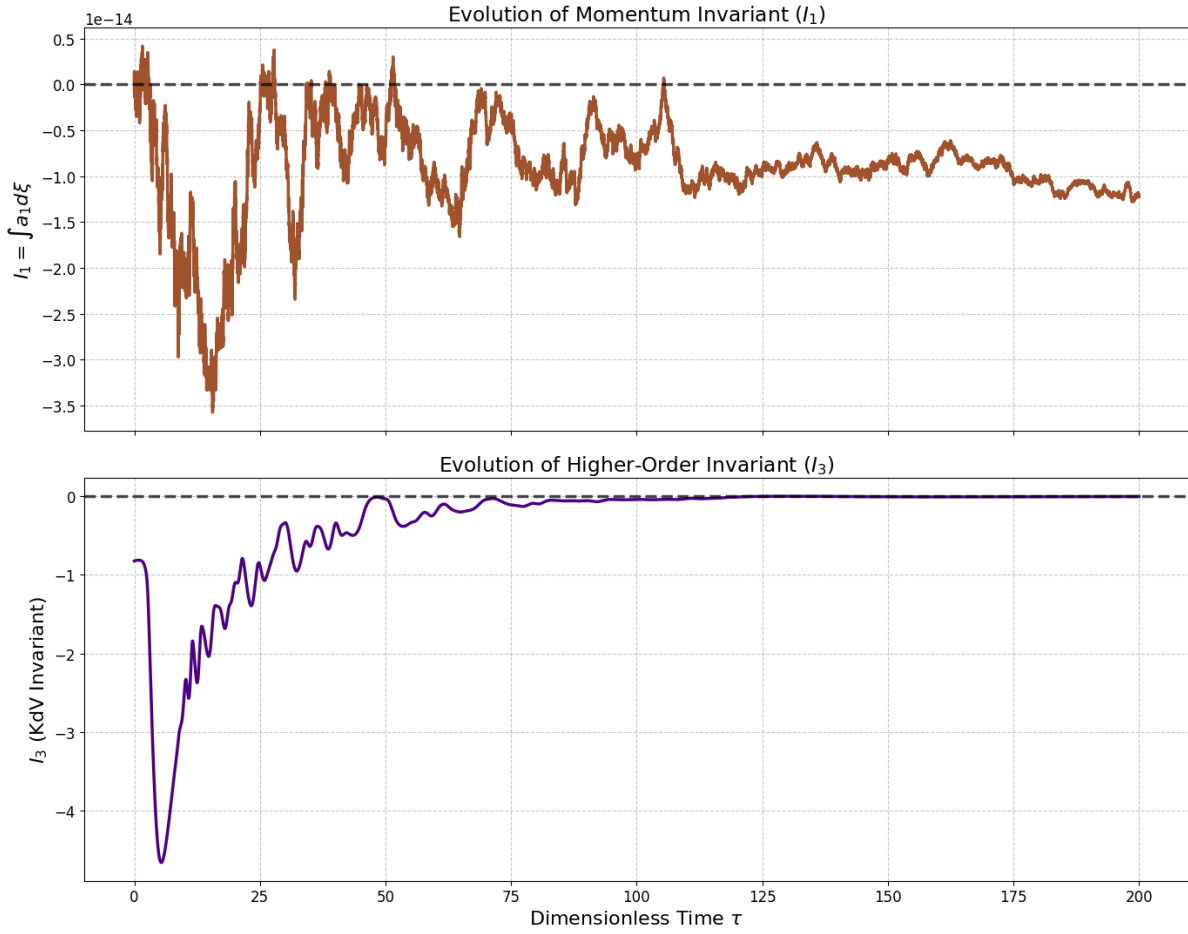


Figure 5: Evolution of the classical KdV invariants for  $Wo = 10$ . Top: Momentum invariant  $I_1$ . Bottom: Higher-order invariant  $I_3$ . The non-constant behavior indicates a non-conservative system.

but the width and energy content at high wavenumbers are maximized for the  $Wo = 15$  case, while the spectrum for  $Wo = 2$  is the most narrowly concentrated at low wavenumbers.

A continuous visualization of these parametric trends is provided in Figure 9. The top panel displays the final waveform structure as a heatmap, where the vertical axis represents the Womersley number. The transition from large-scale, high-amplitude coherent structures at low  $Wo$  to smaller, more complex, and lower-amplitude patterns at high  $Wo$  is evident. Similarly, the bottom panel shows the final power spectrum structure. This visualization clearly illustrates the progressive widening of the power spectrum as  $Wo$  increases from 2 to 15, followed by a global suppression of power at  $Wo = 20$ , confirming the resonant nature of the spectral broadening and the dominant effect of damping at high frequencies.

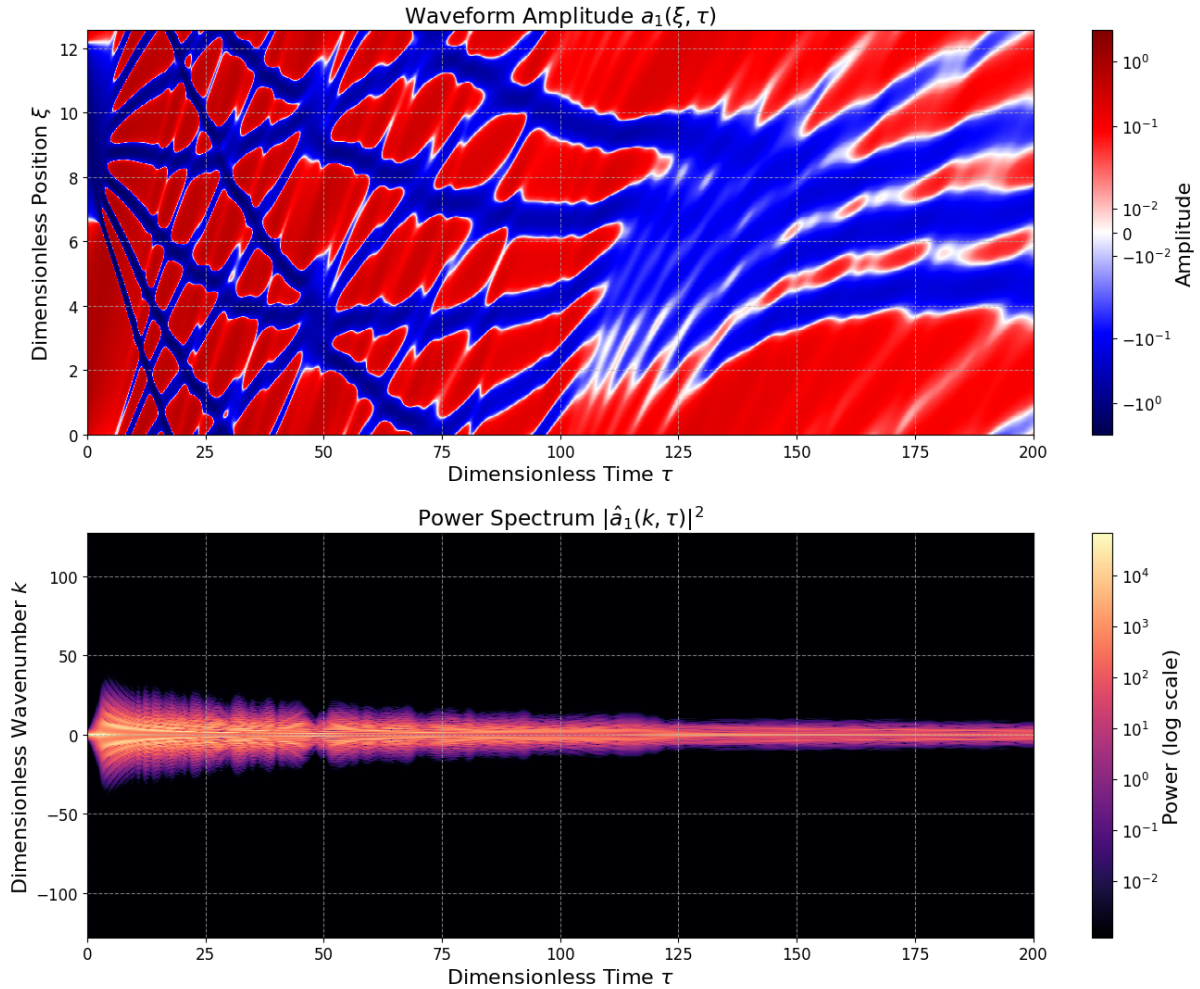


Figure 6: Spatiotemporal evolution of the wave and its spectrum for  $Wo = 10$ . Top: Waveform amplitude  $a_1(\xi, \tau)$  as a function of space and time. Bottom: Power spectrum  $|\hat{a}_1(k, \tau)|^2$  as a function of wavenumber and time.

## Discussion

This study was designed to investigate the role of arterial geometry in the stability of pulsatile flow, specifically to determine if geometric features can actively drive instability. The comprehensive results from the numerical experiments, spanning a range of physiological Womersley numbers, provide a nuanced and physically rich answer. While the system does not exhibit exponential, runaway instability for the tested parameter regime, the findings conclusively establish that geometry functions as a powerful spectral catalyst. It actively and selectively generates flow complexity by governing a competition between parametric forcing, nonlinear dynamics, and frequency-dependent dissipation. A complete, evidence-based account of this mechanism can be constructed by addressing a sequence of logical inquiries that systematically

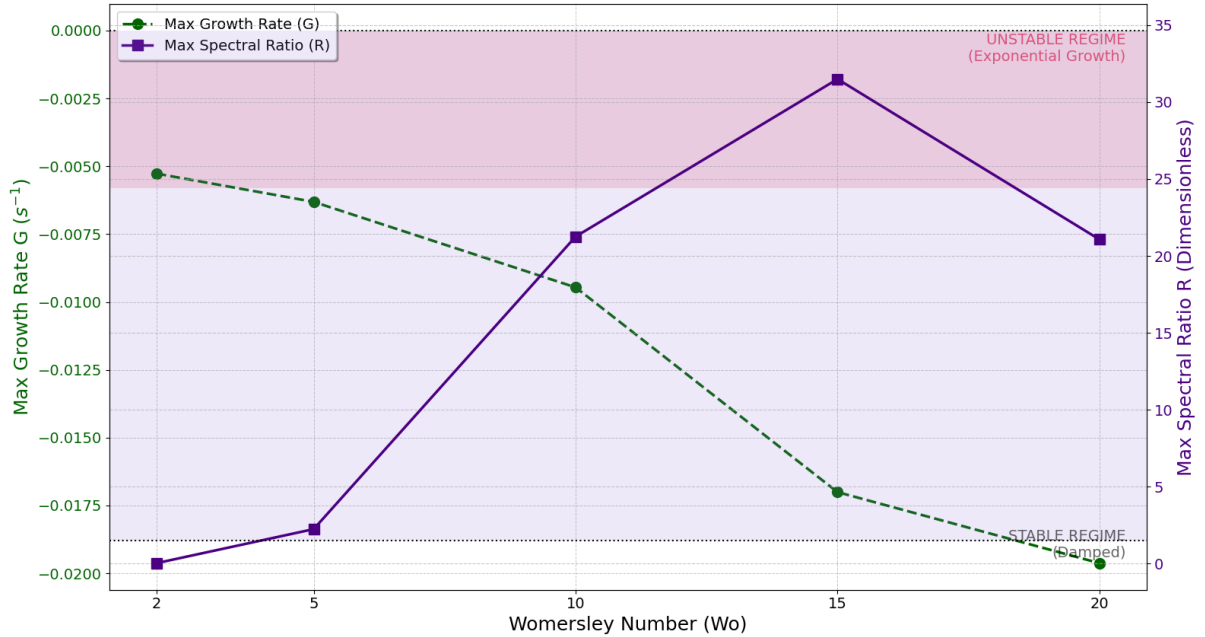


Figure 7: Summary of instability metrics from the parameter sweep versus Womersley number ( $Wo$ ). The maximum late-stage growth rate ( $G$ , left axis, green dashed line) remains negative for all cases. The maximum transient spectral broadening ratio ( $R$ , right axis, purple solid line) shows a peak at an intermediate Womersley number. Shaded regions denote the regimes of exponential growth ( $G > 0$ ) and broadband spectral cascade ( $R > 1.5$ ).

connect the observed results to the underlying mathematical model.

First, what is the fundamental role of geometry within this theoretical framework? The system is modeled by the variable-coefficient fKdV equation, where the influence of geometry is explicitly encoded in the spatially-varying coefficients  $\beta(\xi)$  and  $\eta(\xi)$ . A key finding, shown in Figure 5, is the non-conservation of the classical KdV invariants,  $I_1$  and  $I_3$ . In a constant-coefficient system, these quantities would be strictly conserved, and their fluctuating behavior here is the definitive mathematical proof that the system is being actively forced by the geometry. This validates the central premise of the model: geometry is not a passive boundary condition but an active agent that continuously modulates the integral properties and energy distribution of the flow, a concept motivated by fractional modeling theory [18, 19].

Given that the system is actively forced but remains globally stable—with a negative energy growth rate  $G$  across all tested Womersley numbers (Figure 7)—what is the primary physical consequence of this forcing? The results demonstrate that the forcing drives a highly efficient, transient spectral cascade. This is observed directly as the rapid peak in the spectral broadening ratio  $R$  (Figure 2) and is visualized as the breakdown of the initially smooth waveform (Figure 1) into a field of complex, high-frequency structures (Figure 4 and 6). This process,

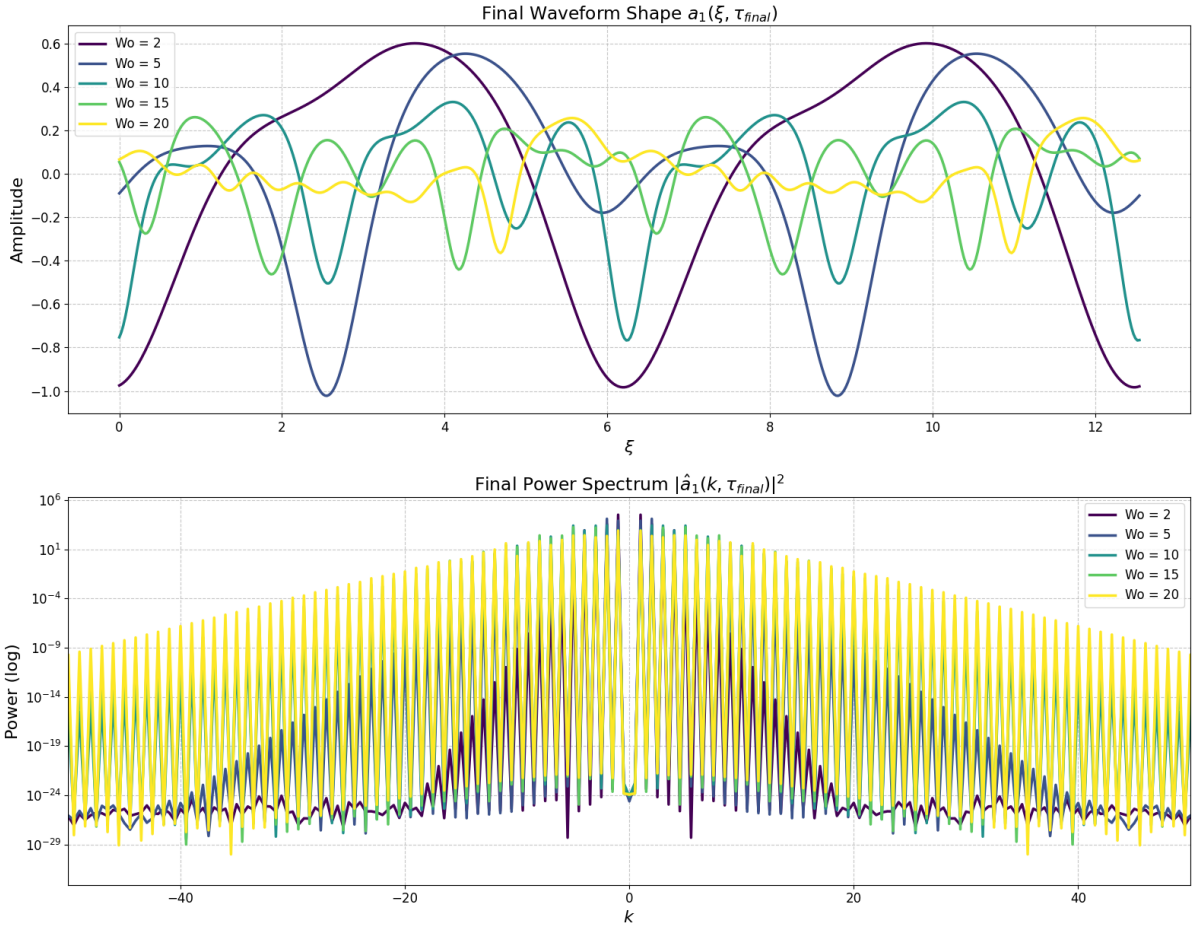


Figure 8: Parametric comparison of final states from the sweep. Top: Overlay of the final waveform shapes,  $a_1(\xi, \tau_{final})$ , for each Womersley number. Bottom: Corresponding overlay of the final power spectra,  $|\hat{a}_1(k, \tau_{final})|^2$ , on a semi-logarithmic scale.

whereby energy is rapidly redistributed from the initial low-wavenumber harmonics to a broad continuum of modes (Figure 3), is governed by the interaction between the nonlinear steepening term,  $\alpha_0 a_1 \partial_\xi a_1$ , and the parametrically-forced dispersive term,  $\beta_0 \varepsilon_\beta \cos(q\xi) \partial_\xi^3 a_1$ . Unlike an integrable system which balances these effects to form stable solitary waves, the spatial variation of  $\beta(\xi)$  constantly disrupts this balance, preventing the formation of stable structures and instead promoting a chaotic-like state of high complexity. This provides a clear, reduced-order physical mechanism for the geometry-induced unsteadiness reported in other computational models [3, 12], and is consistent with the non-Kolmogorov spectral cascades and near-wall coherent structures observed in our prior high-fidelity simulations of patient-specific neurovascular geometries [6, 21].

How does the Womersley number, a parameter of the underlying base flow, regulate this geometrically-driven process? The parameter sweep results in Figure 7 reveal a distinct dual

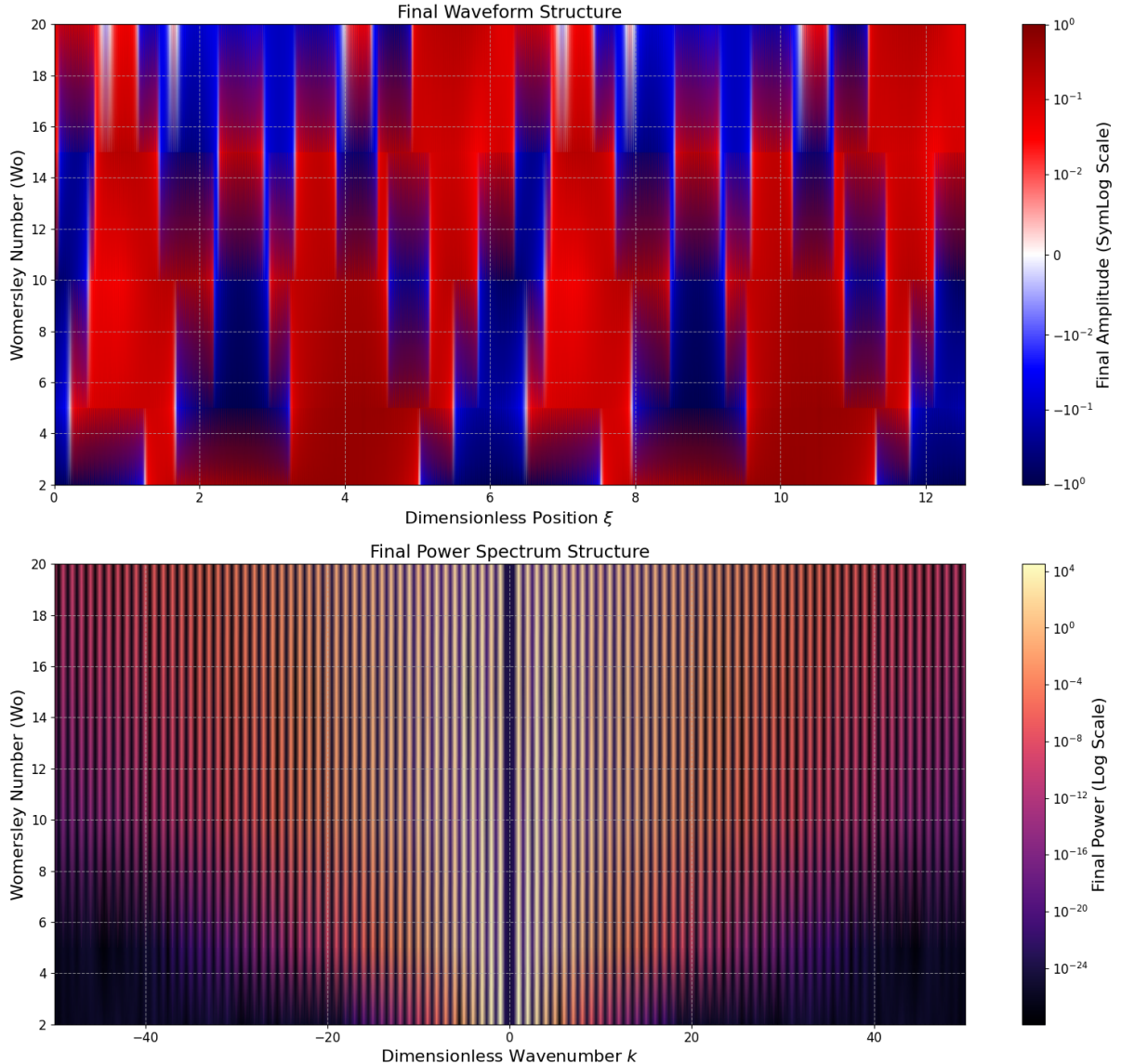


Figure 9: Parametric structure of final states represented as heatmaps. The vertical axis in both plots is the Womersley number. Top: The final waveform amplitude as a function of spatial position  $\xi$ . Bottom: The final power spectrum as a function of wavenumber  $k$ .

role for  $\text{Wo}$ . On one hand, it governs the overall rate of dissipation, as seen by the increasingly negative growth rate  $G$  at higher  $\text{Wo}$ . On the other hand, it critically tunes the efficiency of the spectral cascade. The non-monotonic, resonant behavior of the spectral ratio  $R$ , which peaks at an intermediate value of  $\text{Wo} = 15$ , is the key evidence for this tuning. The mathematical basis for this resonance is the scaling of the baseline dispersion coefficient,  $\beta_0 \propto \text{Wo}^{-2}$ , as defined in the ‘Methods’. As  $\text{Wo}$  increases, the intrinsic dispersion of the wave weakens, making it more susceptible to nonlinear steepening and parametric forcing. The peak at  $\text{Wo} = 15$  thus

represents an optimal matching between the wave's intrinsic timescale, set by  $\text{Wo}$ , and the fixed spatial period of the geometric forcing, set by the wavenumber  $q$ . Conceptually, this behavior is analogous to the resonant "tongues" predicted by Floquet stability theory for parametrically forced systems [17], where instability is maximized at specific forcing frequencies.

This leads to a non-intuitive but critical observation when examining the final, asymptotic states of the system. How can the most spectrally energetic and complex state at  $\text{Wo} = 15$  result in a physical waveform with a lower peak amplitude than the simpler state at  $\text{Wo} = 2$ ? The parametric structure plots in Figure 9 provide the definitive answer. The apparent paradox is resolved by distinguishing between energy concentration and energy distribution. At low  $\text{Wo}$ , the spectral cascade is inefficient; energy remains concentrated in the first few low-wavenumber modes, manifesting as simple, large-amplitude coherent waves. At the resonant peak of  $\text{Wo} = 15$ , the cascade is maximally efficient, shattering the initial wave and distributing its energy across a vast range of high-frequency modes. While the total spectral energy is high, its distribution among many small-scale, out-of-phase structures results in a lower peak physical amplitude, analogous to how broadband white noise has a lower peak pressure than a powerful, low-frequency pure tone of the same total acoustic power.

Finally, what happens at very high Womersley numbers, causing the trend to reverse after the resonant peak? The answer lies in the second role of  $\text{Wo}$ : controlling damping. As seen across all parametric plots (Figures 7, 8, and 9), the solution at  $\text{Wo} = 20$  is significantly attenuated. At these high frequencies, the damping term  $\eta(\xi)(-\partial_\xi^2)^{\frac{1+\gamma_0}{2}} a_1$  becomes highly effective at dissipating the very small-scale structures that the resonant cascade efficiently creates. The final state of the system is therefore a snapshot of the dynamic equilibrium reached between the rate of complexity generation, tuned by the dispersive properties, and the rate of complexity dissipation, governed by the damping properties.

It is important to acknowledge the limitations of the present model. By design, our framework isolates geometry as the sole parametric forcing agent and assumes a rigid wall. Our prior experimental work has shown that wall compliance can have a significant, often attenuating, effect on the kinetic energy cascade and near-wall velocity oscillations in aneurysm models [4,5]. Therefore, a complete picture of hemodynamic stability requires understanding the interplay between the geometry-driven spectral cascade identified here and the dissipative or modulating effects of wall elasticity. Future work should aim to incorporate wall compliance into this reduced-order framework, potentially as a time-dependent or nonlocal damping term, to explore this competitive dynamic.

# Conclusion

Arterial geometry, when modeled as parametric forcing, acts as a resonant, frequency-dependent spectral catalyst. For the studied parameters, it does not cause runaway exponential instability but instead fundamentally alters the character of the flow by efficiently generating small-scale complexity, a process whose efficiency is maximized at a specific resonant Womersley number. The Womersley number plays a dual role: it tunes the system towards this spectral resonance by controlling dispersion, while simultaneously governing the ultimate dissipation of the resulting small-scale structures. While this 1D model is a simplification of the full 3D problem, it successfully isolates this fundamental physical mechanism, providing a quantitative framework for understanding how geometry can be an active and crucial participant in determining the stability and structural complexity of hemodynamic and other complex internal flows.

# Code Availability

The simulation code, including scripts for numerical integration and data analysis, is publicly available on Google Colab at the following URL: [https://colab.research.google.com/drive/1j\\_mJpn\\_j4BUD4DVZNpbGee1YAF2bKS\\_y](https://colab.research.google.com/drive/1j_mJpn_j4BUD4DVZNpbGee1YAF2bKS_y). All data generated during the parametric sweep, along with the detailed simulation results for individual Womersley numbers, are archived in the corresponding repository and can be accessed via the linked notebooks.

# Nomenclature

---

Symbol	Units	Description
<b>Physical Variables and Parameters</b>		
$A(x, t)$	Varies	Physical wave amplitude (e.g., of cross-sectional area or flow rate).
$\mathbf{v}$	m/s	Fluid velocity vector.
$v_z, v_r$	m/s	Axial and radial velocity components in cylindrical coordinates.
$p$	Pa	Pressure.
$t$	s	Time.
$x, z$	m	Axial spatial coordinate.
$\rho$	kg/m <sup>3</sup>	Fluid density.

---

Continued on next page

**Table 2 – continued from previous page**

Symbol	Units	Description
$\mu$	Pa·s	Dynamic viscosity.
$\nu$	$\text{m}^2/\text{s}$	Kinematic viscosity ( $\nu = \mu/\rho$ ).
$R_0$	m	Characteristic vessel radius.
$\omega$	rad/s	Angular frequency of pulsation.
$C(x), D(x), K(x)$	Varies	Spatially-varying physical coefficients for nonlinearity, dispersion, and fractional effects.
$\gamma_0$	–	Constant order of the Riesz fractional operator.

**Dimensionless Variables and Parameters**

$a_1(\xi, \tau)$	–	Dimensionless wave amplitude.
$\xi$	–	Dimensionless axial coordinate.
$\tau$	–	Dimensionless time.
$\text{Wo}$	–	Womersley number, ratio of unsteady inertial to viscous forces.
$A_0, L_0, T_0$	Varies, m, s	Reference scales for amplitude, length, and time used in nondimensionalization.
$\alpha(\xi)$	–	Dimensionless, spatially-varying coefficient for nonlinearity.
$\beta(\xi)$	–	Dimensionless, spatially-varying coefficient for dispersion.
$\eta(\xi)$	–	Dimensionless, spatially-varying coefficient for the fractional term.
$\alpha_0, \beta_0, \eta_0, \gamma_0$	–	Baseline (constant) values of the dimensionless coefficients.
$\varepsilon_i$	–	Modulation amplitudes for the geometric coefficients ( $i \in \{\alpha, \beta, \eta\}$ ).
$q$	–	Dimensionless geometric wavenumber.
$L_g$	–	Dimensionless length of the computational domain.
$k_0$	–	Fundamental dimensionless wavenumber for the initial condition.

**Mathematical and Numerical Symbols**

$\mathcal{D}^{\gamma_0}$	–	Riesz fractional derivative operator of constant order $\gamma_0$ .
--------------------------	---	---

Continued on next page

**Table 2 – continued from previous page**

Symbol	Units	Description
$\mathcal{L}, \mathcal{N}$	–	Continuous linear and nonlinear operators.
$\mathbf{L}$	–	Discretized linear operator (matrix form).
$\hat{a}_1(k)$	–	Fourier transform of the dimensionless amplitude $a_1(\xi)$ .
$k$	–	Dimensionless wavenumber in Fourier space.
$\Delta\tau, \Delta\xi$	–	Time step and spatial grid spacing for numerical simulation.
$N$	–	Number of spatial collocation points.
$I_1, I_2, I_3$	–	Conserved quantities (invariants) of the classical KdV equation.
$G$	–	Instantaneous growth rate of the wave energy ( $I_2$ ).
$R$	–	Spectral broadening ratio (high-frequency to low-frequency energy).

## References

- [1] K. M. Saqr, S. Tupin, S. Rashad, T. Endo, K. Niizuma, T. Tominaga, and M. Ohta, “Physiologic blood flow is turbulent,” *Scientific Reports*, vol. 10, no. 1, 15492, 2020.
- [2] S. A. Mahrous, N. A. C. Sidik, and K. M. Saqr, “Numerical study on the energy cascade of pulsatile Newtonian and power-law flow models in an ICA bifurcation,” *PLOS ONE*, vol. 16, no. 1, e0245775, 2021.
- [3] N. Freidoonimehr, A. F. Fardin, and M. Molla, “Effect of artery curvature on the coronary fractional flow reserve: a computational study,” *Phys. Fluids*, 33:031906, 2021.
- [4] R. Yamaguchi, G. Tanaka, N. S. Shafii, K. B. Osman, Y. Shimizu, K. M. Saqr, and M. Ohta, “Characteristic effect of wall elasticity on flow instability and wall shear stress of a full-scale, patient-specific aneurysm model in the middle cerebral artery: An experimental approach,” *Journal of Applied Physics*, vol. 131, no. 18, 184701, 2022.
- [5] S. Tupin, K. M. Saqr, and M. Ohta, “Effects of wall compliance on multiharmonic pulsatile flow in idealized cerebral aneurysm models: comparative PIV experiments,” *Experiments in Fluids*, vol. 61, no. 7, 172, 2020.

- [6] K. M. Saqr, K. Kano, S. Rashad, K. Niizuma, Y. Kaku, T. Iwama, and T. Tominaga, “Non-Kolmogorov turbulence in carotid artery stenosis and the impact of carotid stenting on near-wall turbulence,” *AIP Advances*, vol. 12, no. 1, 015118, 2022.
- [7] L. Talbot and K. O. Gong, “Pulsatile entrance flow in a curved pipe,” *J. Fluid Mech.*, 127:1–25, 1983.
- [8] C. C. Hamakiotes and S. A. Berger, “Fully developed pulsatile flow in a curved pipe,” *J. Fluid Mech.*, 195:23–55, 1988.
- [9] M. Sumida, K. Sudou, and T. Takami, “Pulsating flow in curved pipes: 2nd report, experiments,” *Bull. JSME*, 27(234):2714–2721, 1984.
- [10] F. Chassagne et al., “The effect of Dean, Reynolds, and Womersley number on the flow in a spherical cavity on a curved round pipe,” *Sci. Rep.*, 11:10605, 2021.
- [11] Z. A. Saib, H. M. Albarody, and A. R. A. Aziz, “A review of fluid–structure interaction: blood flow in arteries,” *Eng. Rep.*, 7(5):e13141, 2025.
- [12] J. Yi, B. J. Li, and B. Guo, “Impact of modelling surface roughness in an arterial stenosis model on wall shear stress metrics,” *Fluids*, 7(5):179, 2022.
- [13] D. G. Owen et al., “Assessment of surface roughness and blood rheology on local coronary haemodynamics—A multiscale CFD study,” *Med. Eng. Phys.*, 74:105–115, 2020.
- [14] Y. Saffar, S. Kashanj, D. S. Nobes, and R. Sabbagh, “The Physics and Manipulation of Dean Vortices in Curved Microchannels: A Review,” *Micromachines*, 14(12):2202, 2023.
- [15] P. N. Williamson, J. D. Humphrey, and S. Baek, “Literature Survey for In-Vivo Reynolds and Womersley Numbers of Various Arteries and Implications for Compliant In-Vitro Modelling,” *Cardiovasc. Eng. Technol.*, 15:1007–1027, 2024.
- [16] D. Xu, J. Peixinho, and R. J. Lingwood, “Non-modal transient growth of disturbances in pulsatile and oscillatory pipe flows,” *J. Fluid Mech.*, 919:A16, 2021.
- [17] J. S. Kern, V. Lupi, and D. S. Henningson, “Floquet stability analysis of pulsatile flow in toroidal pipes,” *Phys. Rev. Fluids*, 9:043906, 2024.
- [18] M. A. Bahloul et al., “Fractional-Order Modeling of Arterial Compliance in Vascular Assessment: A Comprehensive Review,” *Front. Cardiovasc. Med.*, 10:1297830, 2023.
- [19] W. F. W. Azmi, M. Z. Mohamad, and A. Q. Mohamad, “Comparative assessment of classical and fractional models for blood flow: A review,” *Comput. Methods Programs Biomed.*, 258:108342, 2025.

- [20] A. Ali and S. Das, “Applications of neuro-computing and fractional calculus to blood flow problems: A review,” *Comput. Biol. Med.*, 172:107607, 2024.
- [21] K. M. Saqr and I. F. Zidane, “On non-Kolmogorov turbulence in blood flow and its possible role in mechanobiological stimulation,” *Scientific Reports*, vol. 12, no. 1, 12213, 2022.